Self-similar propagation of Hermite-Gauss water-wave pulses

Shenhe Fu,[1,2] Yuval Tsur,[1] Jianying Zhou,[2] Lev Shemer,[3] and Ady Arie[1,*]

[1]*Department of Physical Electronics, Faculty of Engineering, Tel-Aviv University, Tel-Aviv 69978, Israel*

[2]*State Key Laboratory of Optoelectronic Materials and Technologies, Sun Yat-sen University, Guangzhou 510275, China*

[3]*School of Mechanical Engineering, Faculty of Engineering, Tel-Aviv University, Tel-Aviv 69978, Israel*

(Received 9 November 2015; revised manuscript received 10 January 2016; published 26 January 2016)

We demonstrate both theoretically and experimentally propagation dynamics of surface gravity water-wave pulses, having Hermite-Gauss envelopes. We show that these waves propagate self-similarly along an 18-m wave tank, preserving their general Hermite-Gauss envelopes in both the linear and the nonlinear regimes. The measured surface elevation wave groups enable observing the envelope phase evolution of both nonchirped and linearly frequency chirped Hermite-Gauss pulses, hence allowing us to measure Gouy phase shifts of high-order Hermite-Gauss pulses for the first time. Finally, when increasing pulse amplitude, nonlinearity becomes essential and the second harmonic of Hermite-Gauss waves was observed. We further show that these generated second harmonic bound waves still exhibit self-similar Hermite-Gauss shapes along the tank.

DOI: 10.1103/PhysRevE.93.013127

I. INTRODUCTION

Self-similar wave propagation refers to a propagating wave that preserves its shape up to a scale factor during propagation, i.e., its temporal or its spatial profile remains similar to the initial form [1], across the entire propagation space. There are many interesting types of wave packets that exhibit such a property in both the linear and the nonlinear regimes. As examples, in the linear approximation, nonspreading (or nondiffracting) wave packets not only preserve their wave profiles but also maintain the exact original scale during evolution, keeping their size unchanged. Perhaps the best known case for a nonspreading wave is the optical Bessel beam, an exact solution to the Helmholtz equation [2,3]. In the framework of quantum mechanics, Berry and Balazs also suggested an exact solution to the Schrödinger equation—the Airy wave packet that exhibits shape preservation while propagating along a parabolic trajectory [4]. Recently, the Airy wave packet was realized experimentally in optics [5], electron microscopy [6], acoustics [7], and hydrodynamics [8,9]. In the nonlinear regime, solitary wave solutions to the nonlinear equations were explored in many areas of physics [1], manifesting the balance between the linear dispersion and the nonlinear self-focusing effects [10]. In addition to solitons, self-similar parabolic wave pulses that are asymptotic solutions for the nonlinear Schrödinger equation were found in the scope of optical pulses propagating in fibers with normal dispersion [11,12]. These parabolic pulses evolve self-similarly, preserving their parabolic shapes, hence avoiding wave breaking even at the high-intensity nonlinear regime [12,13].

In optics, the Gaussian beam has long been understood to be part of a complete and orthogonal set of solutions to the Helmholtz equation in Cartesian coordinates, where higher-order solutions were named Hermite-Gauss (HG) beams [14,15]. These optical beams possess several characteristic features: first, it was shown that HG beams evolve self-similarly in space, maintaining their initial profiles; second, for the same Gaussian width, the higher-order beam width (defined by the square root of the second-order moment) is M times larger than the width of the respective fundamental beam, where M is related to the order of Hermite functions; third, since they form a complete and orthogonal set of solutions, any scalar wave in Cartesian coordinates can be decomposed to a combination of Hermite-Gauss components [15]. Due to these intriguing properties, so far HG beams have been extensively studied in optical vortex generation [16], mode conversion [17], beam shaping [18,19], harmonic generation [20], etc. Surprisingly, although the HG functions have been extensively applied in optics, to our knowledge, their application in hydrodynamics has not been reported up till now, except for studies of the fundamental Gaussian mode. We note that the evolution of an irrotational narrow-banded water-wave field is often described by models like the nonlinear Schrödinger (NLS), or the modified nonlinear Schrödinger (MNLS) equations [21]. In the linear approximation, however, this wave equation is formally equivalent to the paraxial Helmholtz wave equation. In this article, we study theoretically and experimentally for the first time the self-similar propagation dynamics of surface water wave, having Hermite-Gauss envelopes in both the linear and the nonlinear regimes.

Unlike optical measurements which owing to the high carrier frequency usually concentrate on the wave's intensity [8], disregarding the phase, water waves feature both measurable envelope and phase information, allowing us to directly study the carrier-envelope phase evolution of these self-similar Hermite-Gauss wave pulses. As is known, any converging wave acquires an additional axial phase shift, i.e., the Gouy phase anomaly, which was first discovered in optical waves using the interferometric measurement in 1891 [22], later in single-cycle terahertz wave pulses [23], acoustic few-cycle wave pulse [24], and recently electron matter waves [25,26]. Here, the Gouy phase anomaly in a focusing surface water wave is directly measured for the first time in water wave. We also note that, up till now, most of the Gouy phase measurements, e.g., in optical wave packets, were limited to the fundamental Gaussian wave. In this paper, the measurement of Gouy phase of higher-order Hermite-Gauss pulses is also presented.

*ady@eng.tau.ac.il

II. FORMULATION

We first examine theoretically the linear solution of Hermite-Gauss wave pulse on the surface of deep water. Propagation dynamics of surface gravity water wave can be modeled using the modified nonlinear Schrödinger equation, suggested by Dysthe [21]. Following Refs. [27–29], and neglecting the nonlinear effects for sufficiently low wave steepness, the spatial version of this linearized wave equation in its normalized form is given by

$$\frac{\partial A}{\partial \xi} + i\frac{\partial^2 A}{\partial \tau^2} = 0, \tag{1}$$

where A is the pulse envelope, ξ the propagation distance, and τ the elapsed time. The scaled dimensionless variables are related to the physical units according to $\xi = \varepsilon^2 k_0 x, \tau = \varepsilon\omega_0(x/c_g - t)$ and $A = a/a_0$, where $k_0 = 2\pi/\lambda_0$ is the water wave number with λ_0 being the carrier wavelength. The carrier angular frequency ω_0 satisfies the normally deep-water dispersion relation $\omega_0^2 = gk_0$, with g being the gravitational acceleration. Accordingly, the linear group velocity can be expressed as $c_g = d\omega/dk = \omega_0/(2k_0)$. a_0 is the maximum amplitude of the envelope and $\varepsilon = k_0 a_0$ is the characteristic wave steepness. Equation (1) (linear Schrödinger equation) is formally identical to the paraxial Helmholtz wave equation [5] except that the time coordinate in Eq. (1) (describing the temporal dispersion) is replaced by the space coordinate (describing the spatial diffraction). Taking advantage of such an analogy, we extend the concept of optical Hermite-Gauss beams to hydrodynamics. To look for the Hermite-Gauss solutions of Eq. (1), we assume that the water-wave envelopes at $x = 0$ have the following forms:

$$A(x=0,t) = H_m\left(\frac{\sqrt{2}t}{t_0}\right)\exp\left[-\frac{(1+iC)t^2}{t_0^2}\right], \tag{2}$$

where H_m represents the Hermite polynomial of order m, t_0 is the characteristic envelope duration, and C is used to quadratically modulate the phase of the incident pulses, so that the envelope A becomes linearly frequency chirped. The quadratic phase term $\exp(-iCt^2/t_0^2)$ in Eq. (2), similar to the optical lens transfer function which can focus or defocus a light beam in free space [30], can make the pulses converging or diverging in time during propagation. For instance, when $C < 0$, i.e., the pulse is linearly negative chirped, the front part of the pulse propagates at a group velocity smaller than that of the latter part, leading to pulse focusing in time. Another explanation for pulse focusing is that the induced anomalous dispersion from the negative chirped pulse compensates the normal dispersion through propagation.

Integrating Eq. (1) with the initial condition Eq. (2) yields

$$A(\xi,\tau) = A_0(\xi)H_m(\xi,\tau)\exp\left[-\frac{\mu_0\tau^2}{T^2(\xi)}\right]\exp[i\psi(\xi,\tau)], \tag{3}$$

where

$$A_0 = [T(\xi)]^{-(2m+1)/2},$$
$$\psi = \frac{2m+1}{2}\arctan\left(\frac{4\mu_0\xi}{1+4\mu_1\xi}\right) - \frac{\left(4\mu_0^2\xi+\mu_1+4\mu_1^2\xi\right)\tau^2}{T^2(\xi)}, \tag{4}$$

is the variation of envelope amplitude and phase, respectively. Here $T(\xi) = \sqrt{(1+4\mu_1\xi)^2 + 16\mu_0^2\xi^2}$, $\mu_0 = 1/(\varepsilon\omega_0 t_0)^2$ is constant, and $\mu_1 = C/(\varepsilon\omega_0 t_0)^2$ is related to the chirp coefficient. Equation (4) clearly shows the slowly decreasing pulse amplitude with the location; while the carrier-envelope phase $\psi(\xi,\tau)$ demonstrates a quadratic dependence on time, indicating that the pulse becomes rapidly chirped during evolution. $H_m(\xi,\tau)$ represents the propagated Hermite polynomial and can be expressed analytically as

$$\begin{aligned}
&H_0(\xi,\tau) = 1,\\
&H_1(\xi,\tau) = -2\sqrt{2}\mu_0^{\frac{1}{2}}\tau,\\
&H_2(\xi,\tau) = 8\mu_0\tau^2 - 2[T^2(\xi)],\\
&H_3(\xi,\tau) = -16\sqrt{2}\mu_0^{\frac{3}{2}}\tau^3 + 12\sqrt{2}\mu_0^{\frac{1}{2}}\tau[T^2(\xi)].
\end{aligned} \tag{5}$$

Note that the derivations above were represented in a system traveling at the group velocity c_g. Here the Hermite functions of order m ($m = 0-3$) are considered. Clearly, $H_m(\xi,\tau)$ are real functions, maintaining their Hermite polynomial forms along the propagation distance. Therefore, it is suggested from Eq. (3) that for both the chirped and nonchirped wave pulses, their canonical Hermite-Gauss shapes are preserved, exhibiting self-similar propagation along the wave tank.

Interestingly, in addition to the self-similar propagation property, these HG pulses also experience a phase anomaly, i.e., the Gouy phase [22], given by

$$\psi_G(\xi) = \frac{2m+1}{2}\arctan\left(\frac{4\mu_0\xi}{1+4\mu_1\xi}\right). \tag{6}$$

It shows that in order to observe a significant Gouy phase shift, an initially negative chirp needs to be imposed to such HG wave pulses. In this case, $\mu_1 < 0$, and the value of $4\mu_0\xi/(1+4\mu_1\xi)$ varies from $-\infty \to \infty$ for $\xi = 0 \to \infty$, giving rise to the Gouy phase shift of $(m+\frac{1}{2})\pi$. The fundamental mode, i.e., the HG_0 pulse, experiences a Gouy phase shift of $\frac{\pi}{2}$, while the higher-order modes, HG_1, HG_2, and HG_3 waves, undergo Gouy phase shifts of $\frac{3\pi}{2}$, $\frac{5\pi}{2}$, and $\frac{7\pi}{2}$, respectively. The Gouy phase anomaly becomes less significant for a nonchirped ($\mu_1 = 0$) or positively chirped ($\mu_1 > 0$) pulse. This is because the value of $4\mu_0\xi/(1+4\mu_1\xi)$ only varies from 0 to $+\infty$ for $\xi = 0 \to \infty$. Thus, the phase shift of ψ_G is $(2m+1)\pi/4$, half of the phase shift from the chirped pulses. In both cases, the higher-order HG pulses accumulate Gouy phase $2m+1$ times as quickly as the fundamental mode; see Eq. (6).

III. RESULTS

A. Linear propagation dynamics

Our experiments were performed in an 18-m-long and 1.2-m-wide laboratory wave flume with a constant water depth $h = 0.6$ m. Surface gravity Hermite-Gauss waves were generated by means of a computer controlled paddle-type wave maker installed at one end of the wave flume. To avoid wave reflections, an absorbing beach of 3 m long was installed at the opposite end; see detailed information of experimental setup in Ref. [31]. The beach reduces considerably the amplitude of the reflected waves. Therefore, our measurement was limited up

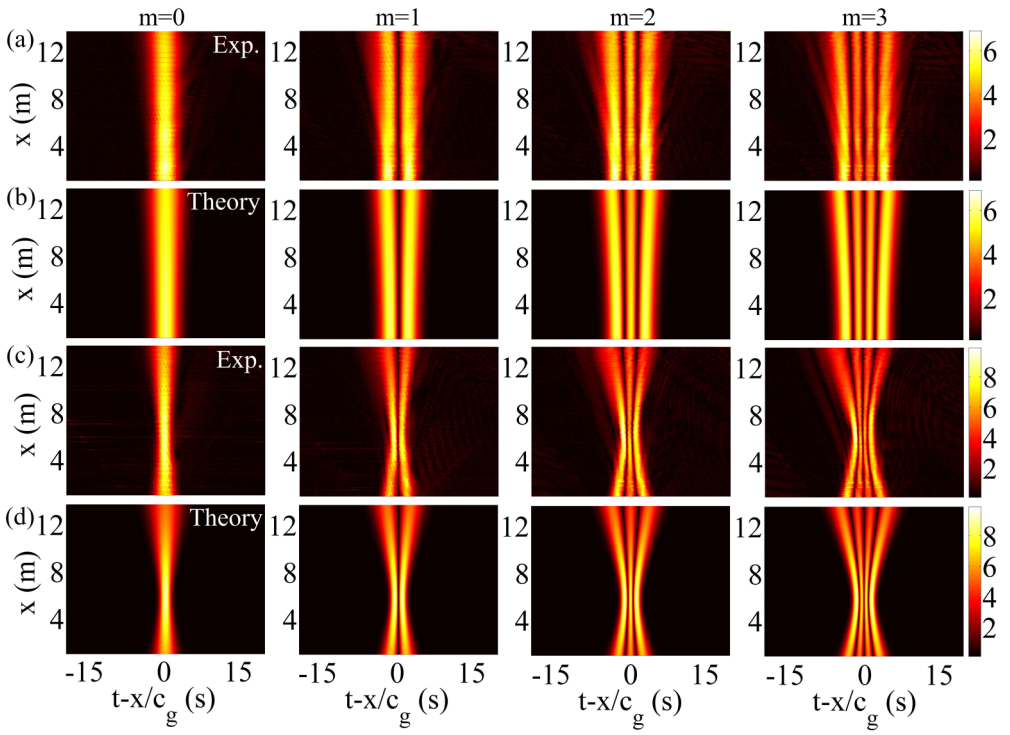

FIG. 1. The envelope evolutions of the nonchirped and linearly chirped Hermite-Gauss wave pulses, with parameters of a_0=6 mm, $t_0 = 2.5$ s, and $C = 0$ (a, b), $C = -2.19$ (c, d) for different order of m (see the top). In the experiments, the pulse envelopes were obtained using Hilbert transform of the measured elevations, in a frame of reference moving at speed c_g. The color bar units of the envelope are millimeters. (a, c) The experimental measurements and (b, d) the theoretical results based on Eq. (3).

to a distance of 14 m from the wave maker. The instantaneous surface elevation at any fixed location along the tank was measured by four wave gauges with a sampling frequency of 400 Hz. These wave gauges were mounted on a bar parallel to the propagation direction. The bar with the gauges is fixed to an instrument carriage that can be shifted along the tank and is controlled by the computer. The temporal surface elevation wave groups generated by the wave maker takes the following form:

$$\eta(x = 0,t) = a_0 A(x = 0,t)\cos(\omega_0 t). \tag{7}$$

Here the maximum value of $A(x = 0,t)$ is normalized to unity so that a_0 is the maximum amplitude of the envelope. In the experiment, the carrier wavelength was selected as $\lambda_0 = 0.76$ m, so that the dimensionless depth $k_0 h = 4.96 > \pi$ satisfied the deep-water condition [32]. In this case, the wave dissipation can be neglected.

To experimentally visualize these HG wave pulses, the characteristic envelope duration was set to $t_0 = 2.5$ s, and the amplitude $a_0 = 6$ mm ($\varepsilon = 0.05$). In this case, the nonlinear effects could be neglected. Figure 1 illustrates the experimental [see Figs. 1(a) and 1(c)] and theoretical [see Figs. 1(b) and 1(d)] envelope evolutions of the nonchirped ($C = 0$) and linearly chirped ($C = -2.19$) pulses along the water flume, with different orders ($m = 0$–3). In the experiments, the pulse envelopes were obtained by Hilbert transforming the recorded wave elevations, represented in a comoving system with a group velocity of c_g. In both cases (the chirped and nonchirped pulses), it was observed that these HG pulses propagate self-similarly along the wave flume, preserving their initial HG shapes. Our experimental measurements are supported by the theory based on Eq. (3). For the nonchirped pulses, see Figs. 1(a) and 1(b), due to large dispersion length $x_0 = gt_0^2/4 \simeq 15$ m, the HG_0 pulse exhibits only a weak dispersion while traveling throughout the tank, keeping its temporal width almost unchanged. However, relative spreading of higher-order pulses was observed. The higher-order HG pulses broaden more significantly than the fundamental Gaussian pulse. For the chirped pulses, see Figs. 1(c) and 1(d), owing to the introduced negative chirp that compensates the normally inherent dispersion, these pulses converge to a minimum temporal size at the location of $x \sim 6$ m and then diverge significantly after passing the focus.

We note that, for the chirped pulses, the elevation wave groups remain negatively chirped before the focus, thereby converging the pulses during propagation. At the focal spot, these waves can be considered as nonchirped pulses; while after the focus, they become positively chirped and start diverging. This evolution pattern is similar to that observed for focused wave groups in Ref. [32]. The phenomenon was observed directly by measuring pulses' temporal elevations at three typical locations in the tank; see Fig. 2. It demonstrates clearly the transition from negatively chirped pulses (see the elevations at $x = 1$ m) to positively chirped pulses (see the elevations at $x = 11$ m) for three higher-order HG pulses. We also point out that few cycle water-wave pulses were generated near the focal location of the tank (see the elevations at $x = 6$ m), suggesting that these linearly chirped pulses were efficiently compressed. We constructed the pulse envelopes using the Hilbert transform (see the blue curves in Fig. 2),

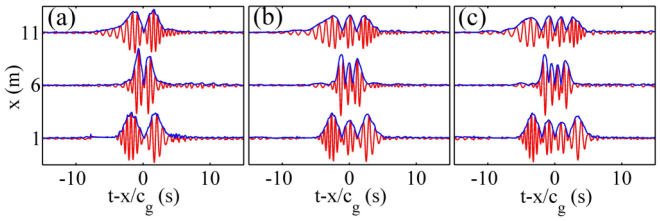

FIG. 2. The temporal profiles of the measured elevation wave groups at $x = 1$ m (before the focus), 6 m (nearly the focus), and 11 m (after the focus), with different orders: (a) $m = 1$, (b) $m = 2$, and (c) $m = 3$. The parameters are set as $a_0 = 6$ mm, $t_0 = 2.5$ s, and $C = -2.19$. Red curves are the measured elevations while the blue curves denote the constructed envelopes by Hilbert transform.

showing excellent Hermite-Gauss profiles. The envelopes at $x = 1$ m and $x = 11$ m remain almost the same, owing to the symmetry of these two locations with respect to the focal point ($x \simeq 6$ m).

In order to describe HG pulses' propagation quality, their square root of the second-order moment along the tank was measured using the expressions [8]

$$\sigma_m(x) = \left[\frac{4\int_{-\infty}^{\infty}(t-\bar{t})^2|\eta|^2dt}{\int_{-\infty}^{\infty}|\eta|^2dt}\right]^{\frac{1}{2}}, \quad \bar{t} = \frac{\int_{-\infty}^{\infty}t|\eta|^2dt}{\int_{-\infty}^{\infty}|\eta|^2dt}, \qquad (8)$$

where $\sigma_m(x)$ denotes the square root of the second moment of HG pulses with order m ($m = 0 - 3$) at location of x. Figures 3(a) and 3(b) show the outcomes for the nonchirped [see Fig. 3(a)] and chirped [see Fig. 3(b)] pulses, respectively. The solid lines correspond to the theoretical results while the scattered dots represent the experimental outcomes with error bars 5% of the data. For the nonchirped HG pulses we can observe the mild increase of σ_m with increasing x, and higher-order HG pulses broaden slightly faster than lower-order pulses, in accordance with the envelope evolutions

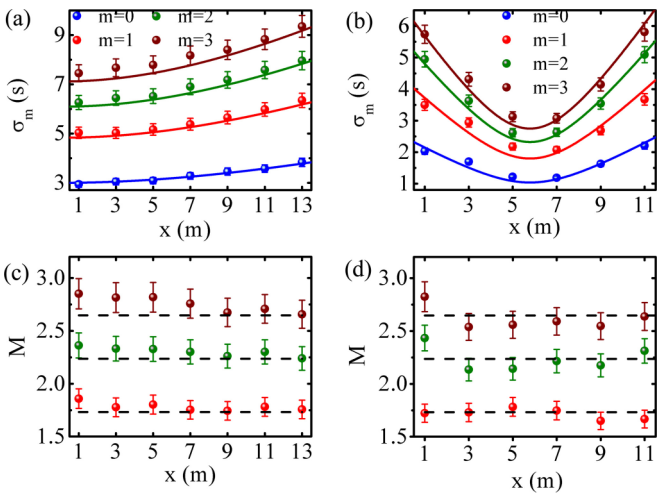

FIG. 3. (a, b) The measured square roots of second-order moments of HG wave pulses, as a function of locations. The parameters used here are $a_0 = 6$ mm, $t_0 = 2.5$ s, and $C = 0$ (a), $C = -2.19$ (b). (c, d) The calculated M factor as a function of locations, with $C = 0$ (c), $C = -2.19$ (d). In all these figures, the lines denote the theoretical results; while the scattered dots represent the experimental outcomes.

illustrated in Fig. 1(a). For the chirped pulses [see Fig. 3(b)], these curves for σ_m exhibit a parabolic-symmetric shape, with their minimum value located at $x \sim 6$ m. Slight difference between the experiment and theory was observed, due to small deviation of the elevation generated by the wave maker, as compared with the theory.

We have already mentioned earlier an important property of a higher-order Hermite-Gauss wave that has a width M ($M=\sqrt{2m+1}$) times larger than the width of a fundamental Gaussian wave for the same Gaussian envelope [14]. We confirmed this property by calculating their M factor defined as $M=\sigma_m/\sigma_0$. The results are plotted in Figs. 3(c) and 3(d) for the nonchirped and chirped pulses, respectively. The data points with an accuracy of 5% show the experimental results and the dashed lines are the expected value for the M factor. It is clearly seen that for both the cases, their square roots of second moments approximately satisfy the relationship $\sigma_m = M\sigma_0$.

B. Phase measurement

The phase of a wave function is usually inaccessible in optical experiments, owing to the high carrier frequency ($\sim 10^{14}$ Hz). However, in our experiments, the measured wave elevations with low carrier frequency allows us to demodulate the envelope phase of these Hermite-Gauss pulses. As recently reported in Ref. [8], the envelope phase of these pulses can be determined by extracting the local maximum and minimum values of the elevations. In the experiments, the envelope phase ψ is modulated by a carrier wave contained in the elevation: $\eta(x,t)=\mathrm{Re}[a_0 A(x,t)\exp(ik_0x - i\omega_0 t)]$. Therefore, the phase of the elevations is described by

$$\varphi(x,t) = \psi(x,t) + \psi_m(x,t) + k_0x - \omega_0 t, \qquad (9)$$

where $\psi_m(x,t)$ is the phase of Hermite functions of order m [see Eq. (5)]. At those particular points, we have the relationship $\cos(\varphi) = \pm 1$ [for the maximum (minimum) points, it equals 1 (-1)]. The induced envelope phase at a fixed location is thus expressed as $\psi + \psi_m = \arccos(\pm 1) + \omega_0 t - k_0 x$.

Using this technique, the envelope phase of HG pulses was determined; see Fig. 4 in the case of nonchirped pulses. Figure 4(a) illustrates theoretically the envelope phase variation with t and x for different orders of HG waves. For clear observation, temporal envelope phase variation at two typical locations of $x = 1$ m and $x = 11$ m were plotted [see Figs. 4(b) and 4(c), respectively], corresponding to the white dashed lines in Fig. 4(a). To avoid phase ambiguity, these results were demonstrated in a form of cosine function, i.e., $\cos(\psi + \psi_m)$. As mentioned before, the envelope phase is a quadratic function of time with Gouy phase offset; see Eq. (4). In this case, owing to the small quadratic chirp coefficient, we observe that for HG_0 pulse (see the figures at $m = 0$), the envelope phase varies slowly with t and x. However, for the higher-order HG pulses, which accumulate Gouy phase $2m + 1$ times faster than the HG_0 pulse, their envelope phase changes significantly. Moreover, the direct phase measurements enable us to observe the π-phase jump of the higher-order pulses, as a consequence of the modulation of Hermite functions. For the HG_1 pulse (see figures at $m = 1$), a single phase jump occurs at $t = 0$; whereas the HG_2 and HG_3 pulses undergo two and three phase jumps, respectively.

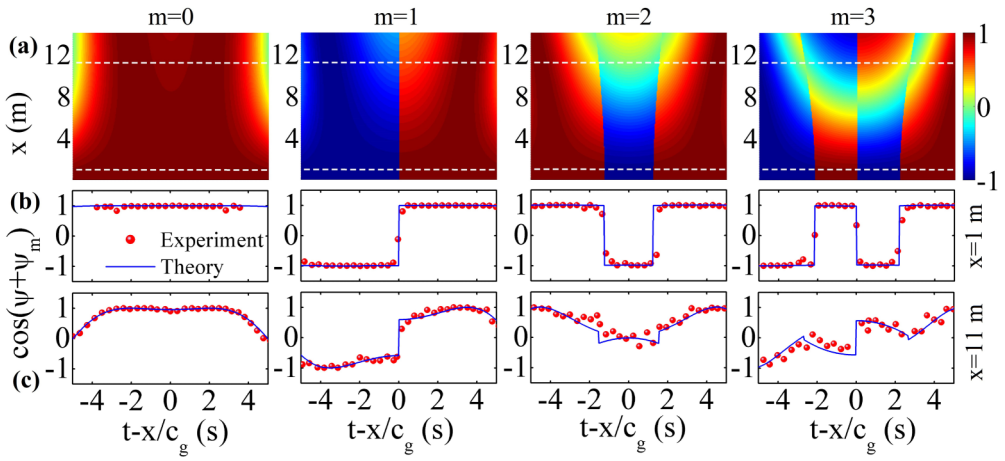

FIG. 4. The carrier-envelope phase of the nonchirped HG pulses demodulated from the measured elevations, with $a_0 = 6$ mm, $t_0 = 2.5$ s, and $C = 0$. The obtained envelope phase was illustrated as a cosine function of time. (a) Two-dimensional phase map calculated from Eq. (3) for different order of m. (b, c) The envelope phase profiles at $x = 1$ m (b) and $x = 11$ m (c). The blue curves in (b) and (c) correspond to the theory, while the red scattered dots denote the experiments.

We further measured the envelope phase of the chirped HG pulses; see Fig. 5. In this case, the introduction of negative chirp strongly affects the pulse propagation, leading to rapid phase variation with t and x, as compared with the nonchirped cases. Figure 5 also plots their theoretical phase variation [see Fig. 5(a)], as well as the temporal phase profiles at $x = 1$ m (before the focus) and $x = 11$ m (after the focus) in Figs. 5(b) and 5(c), respectively. We observed that, in addition to the π-phase jump, for the HG_0 and HG_2 pulses, their envelope phase profiles at $x = 1$ m and $x = 11$ m remain similar; while for the HG_1 and HG_3 pulses, the envelope phase profiles are almost time reversed. This phenomenon is attributed to the phase similarity before and after the focal point.

Another interesting phenomenon of HG water-wave pulses, mentioned above, is the Gouy phase behavior that had been studied extensively in various types of waves such as optical waves [22,23], acoustic waves [24], and matter waves [25,26]. In this work, the Gouy phase measurement of HG water-wave pulses is presented for the first time. Theoretically, the envelope phase ψ has a quadratic dependence of time with the Gouy phase offset, as can be seen from Eq. (4). In the experiments, the demodulated envelope phase can be written as $\psi = \psi_G + \gamma t^2$, where γ (in the unit of radian/s^2) is a quadratic coefficient. Both the value of ψ_G and γ can be obtained directly by fitting the envelope phase with the method of least square. Figure 6 shows the obtained results for both the nonchirped and chirped wave pulses. For the nonchirped pulses [see Fig. 6(a)], it is observed that in all these cases ($m = 0 - 3$) the Gouy phase is increasing slowly with the increase of x. Note that the Gouy phase of HG_0 mode is rather small. For the chirped pulses [see Fig. 6(b)], the value of Gouy phase increases significantly, compared with the nonchirped pulses. Furthermore, the variation of the Gouy phase from $x = 0$ to $x = 13$ m exhibits similar "S" shapes for chirped HG pulses. In both cases, the Gouy phase of higher-order modes is $2m + 1$ times larger than the case of HG_0 mode. As expected, a converging HG_0 wave experiences $\pi/2$ Gouy phase shift when it propagates from $x = 0 \rightarrow +\infty$. However, in the experiment, due to the limited length of the wave tank, the total phase shift for the HG_0 is less than $\pi/2$.

The quadratic coefficient γ describing the pulse chirping was also studied for these pulses; see Figs. 6(c) and 6(d).

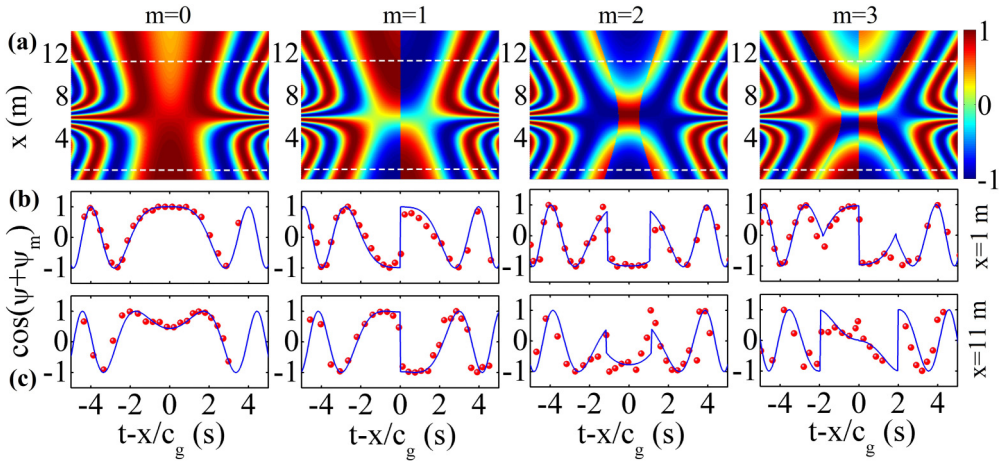

FIG. 5. The same as described in the caption of Fig. 4, but in the case of chirped pulses, i.e., $C = -2.19$.

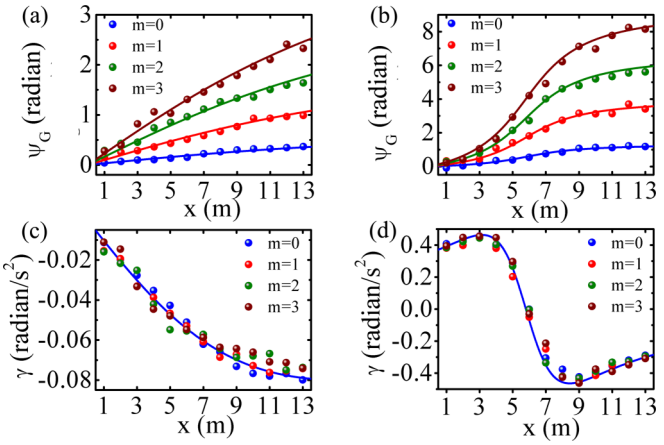

FIG. 6. The obtained Gouy phase ψ_G (a, b) and quadratic coefficient γ (c, d) by fitting the envelope phase with the method of least square. The parameters are set as $a_0 = 6$ mm, $t_0 = 2.5$ s, and $C = 0$ (a, c); $C = -2.19$ (b, d). The scattered data points correspond to the experimental outcomes, while the solid lines represent the theoretical results.

Although no chirping was initially added to the pulses, i.e., $\gamma = 0$ at $x = 0$ [see Fig. 6(c)], these pulses still accumulate positive chirp (owing to the normal dispersion) while propagating along the tank, as can be deduced from the negative value of γ at $x \neq 0$. Owing to the slow increase of γ as a function x, its value remains relatively small throughout the tank, indicating that these pulses exhibit weak spreading during propagation. However, for the negatively chirped pulses, $\gamma > 0$ at $x = 0$; see Fig. 6(d). The value of γ remains positive when $x < \sim 6$ m and becomes negative at $x > \sim 6$ m, experiencing a transition at the location at $x \sim 6$ m. That means these pulses remain negatively chirped before the focus and become positively chirped after passing the focus, in accordance with the results shown in Fig. 2. Owing to the initial chirp at $x = 0$, the value of γ becomes relatively larger, having an inverse "S" shape. We note that γ is independent of the order of HG functions, as shown in Eq. (4). Thus, the obtained γ in all these cases approximately overlap together; see Figs. 6(c) and 6(d), respectively.

C. Second harmonic generation

Finally, we examine both experimentally and numerically nonlinear propagation dynamics of the Hermite-Gauss wave pulses with appreciable amplitude. In this case, the nonlinearity becomes dominant and wave propagation is governed by the modified nonlinear Schrödinger equation [27–29] written in its normalized form,

$$\frac{\partial A}{\partial \xi} + i\frac{\partial^2 A}{\partial \tau^2} + i|A|^2 A + 8\varepsilon|A|^2\frac{\partial A}{\partial \tau} + 2\varepsilon A^2\frac{\partial A^*}{\partial \tau} + 4i\varepsilon A\frac{\partial \Phi}{\partial \tau}\bigg|_{Z=0} = 0, \quad 4\frac{\partial^2 \Phi}{\partial \tau^2} + \frac{\partial^2 \Phi}{\partial Z^2} = 0 \quad (Z < 0), \tag{10}$$

where $Z = \varepsilon k_0 z$ is the scaled vertical coordinate and Φ is the induced velocity potential, which satisfies $\partial\Phi/\partial Z = \partial|A|^2/\partial\tau$ $(Z = 0)$ and $\partial\Phi/\partial Z = 0$ $(Z = -\infty)$. Here A denotes the complex envelope of the first harmonic free waves, while the second harmonic bound waves can be determined using the expression $B = \frac{1}{2}\varepsilon A^2$ [28]. Therefore, the nonlinear elevation wave groups can be expressed as $Ae^{i(k_0 x - \omega_0 t)} + Be^{2i(k_0 x - \omega_0 t)}$. Note that the third harmonic waves are not considered here due to their negligible amplitude. To observe nonlinear effects, we increase the amplitude to $a_0 = 21$ mm ($\varepsilon = 0.17$), keeping other parameters unchanged. Figure 7(a) illustrates experimentally the envelope evolution of nonlinear HG pulses in the case of nonchirped pulses. These HG envelopes consist of the first harmonic free waves and the second harmonic bound waves. It clearly shows that these nonlinear waves still maintain their self-similar propagation despite the strong nonlinearity, approximately preserving their HG shapes. We observed that HG_0 pulse was seriously compressed, suggesting the induced strong nonlinearity. The higher-order pulses were less compressed, due to the smaller width of their lobes as compared with the Gaussian duration. This indicates that higher-order HG pulses are more resilient to nonlinear perturbations. Owing to the nonlinear effects, the propagating group velocity was slightly modified. Consequently, these pulses propagate slightly faster than c_g; see Fig. 7(a).

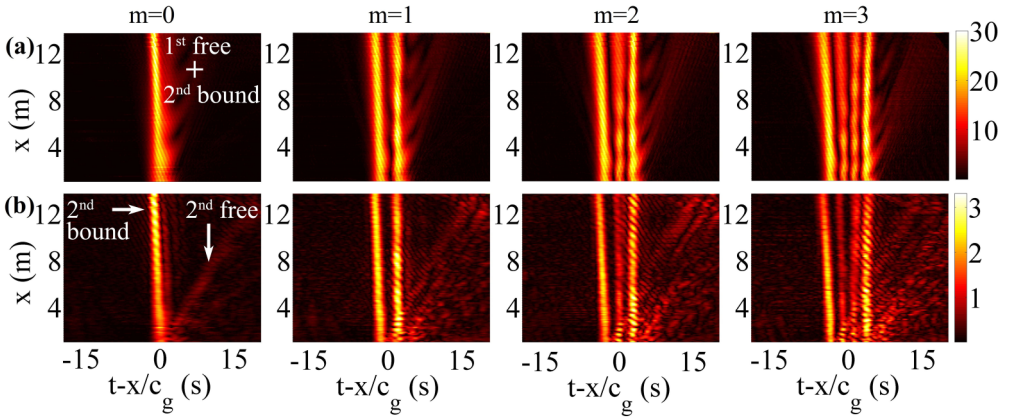

FIG. 7. Experimental results for: (a) nonlinear propagation dynamics of HG pulses and (b) the generated second harmonic bound waves with $a_0 = 21$ mm ($\varepsilon = 0.17$), $t_0 = 2.5$ s, and $C = 0$. Both (a) and (b) represent the envelope in a moving system. The color bar units are millimeters.

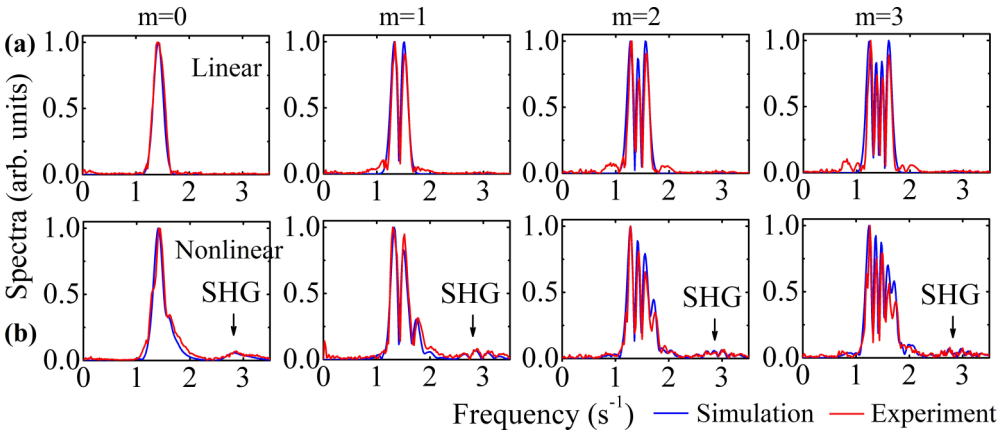

FIG. 8. The spectra of the nonchirped HG wave pulses calculated at the location of $x = 7.39$ m, with $t_0 = 2.5$ s and $C = 0$. (a) The measured linear spectra with a_0=6 mm ($\varepsilon = 0.05$); (b) the measured nonlinear spectra with $a_0 = 21$ mm ($\varepsilon = 0.17$). Blue curves correspond to simulations based on Eq. (10); while the red curves denote the experiments.

To further study the nonlinear effects, we presented here the spectra of nonlinear HG pulses, shown in Fig. 8(b). In comparison, the spectra of linear pulses were also considered; see Fig. 8(a). These spectra in both cases were obtained at a fixed location of $x = 7.39$ m. We compared our experimental pulse spectra with simulations based on Eq. (10), preformed by the split-step Fourier method [27]; see the blue curves, showing a good correspondence. In the linear case [see Fig. 8(a)], in all the cases ($m = 0 - 3$), these spectra are symmetric, also having HG shapes. The center of the fundamental harmonic is located at $f_0 = \omega_0/(2\pi)$. In the nonlinear regime [see Fig. 8(b)], owing to the contribution of second harmonic bound waves [the observation of the second order higher frequency indicates a second harmonic generation (SHG)], these spectra exhibit asymmetry and become wider, which is similar to Refs. [32,33]. Despite the nonlinearity, their general HG shapes could still be recognized in the dominant frequency components. This can explain that in the nonlinear regime, the HG shapes can be approximately preserved during propagation.

In order to obtain an image of the excited second harmonic bound waves along the tank, we extracted the second harmonic spectra in a range of $2f_0 \pm 0.5$ Hz and neglected all other spectra components. The results are shown in Fig. 7(b), illustrating their excited pulse envelopes along the tank. It shows that these generated second-harmonic bound waves at any location of the tank also have similar Hermite-Gauss shapes. In addition, the second-harmonic free waves were also observed, propagating at a smaller velocity of $c_g/4$, as judged from the waves emitted at an angle to the straight vertical line; see the arrow in Fig. 7(b). Due to gradual separation between the bound and the free second harmonic waves along the distance, these second harmonic free waves mix together and therefore their HG shapes are not observed clearly (one technique to avoid this phenomenon is based on the chirp pulses with lower incident amplitude, demonstrated in Fig. 9). From the color bars in Figs. 7(a) and 7(b), we estimated that the SHG efficiency is around 11% (3.3/30 = 0.11). We should mention that, contrary to the nonchirped pulses, generating second harmonics of initially negative chirped Hermite-Gauss waves along the water tank is not straightforward. This is because, the chirped pulses broaden seriously after passing the focus, reducing their amplitude and hence the SHG efficiency. Also, due to the focus effect, the spectra width varies rapidly with the locations, which hinders the extraction of the second harmonic components. A practical conclusion is that adding a chirp to the Gaussian pulse enables us to suppress nonlinear distortions. This concept is often used in optical fiber communication and can become useful in hydrodynamics as well.

Moreover, using the technique of chirp pulses, the second harmonic response can be observed only at chosen regions, i.e., nearly the focal regions in the tank. As a realization, we increase the chirp to $C = -4.11$, and reduce incident amplitude to $a_0 = 8$ mm, setting $t_0 = 3.3$ s. The results are demonstrated both experimentally and numerically, with orders $m = 0, 1$; see Fig. 9. Since the input amplitude is low, the second-harmonic bound waves are negligible before and after the focal regions, see the corresponding spectra at $x = 1.0$ m [see Figs. 9(a) and 9(d)], and at $x = 12.0$ m [see Figs. 9(c) and 9(f)]. However, owing to the strong negative

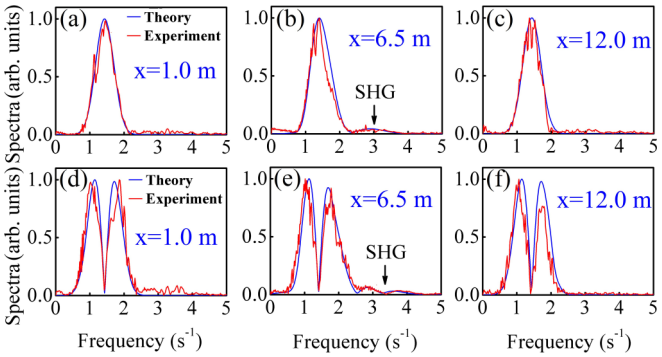

FIG. 9. The spectra of the chirped HG pulses with order (a)–(c) $m = 0$ and (d)–(f) $m = 1$, calculated at three different locations: (a, d) $x = 1.0$ m (before the focus), (b, e) $x = 6.5$ m (near the focus) and (c, f) $x = 12.0$ m (after the focus). The parameters are set as $a_0 = 8$ mm, $t_0 = 3.3$ s, and $C = -4.11$. Blue curves correspond to simulations based on Eq. (10); while the red curves denote the experiments.

chirp, when these pulses propagate to the focal region, they are seriously compressed, increasing their amplitude and hence inducing harmonic bound waves, as seen from the second harmonic components in Figs. 9(b) and 9(e). Our measurements are supported by the numerical outcomes. We also point out that, the introduction of strong chirp gives rise to waves oscillating at faster frequencies, and hence weak dissipation of waves occurs during propagation. Wave dissipation become more pronounced in the higher-order HG wave pulses, as evident from Fig. 9(f).

IV. CONCLUSION

We observed self-similar propagation of Hermite-Gauss water-wave pulses in both the linear and the nonlinear regimes. In the linear regime, we discussed their properties of shape preservation, width variation, and envelope phase evolution along an 18-m water flume. Although the importance of Gouy phase has been demonstrated in various areas of optics [34,35], most of the measurements of Gouy phase are still limited to the Gaussian wave packet; see Refs. [23,24,26], among others. In this work, we performed the Gouy phase measurement of their higher-order counterparts. In the nonlinear regime, we studied nonlinear propagation dynamics of HG wave pulses with appreciable nonlinearity, as well as their generated second-harmonic bound waves along the wave tank. We found that both the first harmonic free waves and the generated second harmonic bound waves exhibit self-similar property. Our experimental results match well with the simulations based on the MNLS equation. The observed asymmetry with respect to the central frequency of the measured spectra as shown in Fig. 8 stems from the two nonlinear terms that are proportional to the square of the amplitude; see Eq. (10). However, our simulations demonstrate that as long as the asymmetry of wave train envelope and of the spectra is not too strong (e.g., in the case of a chirped pulse shown in Fig. 9), the nonlinear Schrödinger equation still could be utilized to simulate nonlinear evolution of surface gravity water waves. We note that although there has been a number of studies demonstrating the applications of HG waves in optics [16–20], to our knowledge, this is the first time that this family of solutions is demonstrated in water waves. We anticipate that many new phenomena still can be explored both in water waves and optical waves, owing to the analogy between their wave equations [8,36,37].

ACKNOWLEDGMENTS

This work was supported by DIP, the German-Israeli Project cooperation, the Israel Science Foundation (Grant No. 1310/13), the National Basic Research Program (Grant No. 2012CB921904), the U.S.-Israel Binational Science Foundation (Grant No. 2010219), and the Overseas Study Program of the China Scholarship Council.

[1] G. I. Barenblatt, *Scaling, Self-Similarity, and Intermediate Asympotics* (Cambridge University Press, Cambridge, 1996).
[2] J. Durnin, J. Opt. Soc. Am. A **4**, 651 (1987).
[3] J. Durnin, J. J. Miceli, Jr., and J. H. Eberly, Phys. Rev. Lett. **58**, 1499 (1987).
[4] M. V. Berry and N. L. Balazs, Am. J. Phys. **47**, 264 (1979).
[5] G. A. Siviloglou, J. Broky, A. Dogariu, and D. N. Christodoulides, Phys. Rev. Lett. **99**, 213901 (2007).
[6] N. Voloch-Bloch, Y. Lereah, Y. Lilach, A. Gover, and A. Arie, Nature **494**, 331 (2013).
[7] P. Zhang, T. Li, J. Zhu, X. Zhu, S. Yang, Y. Wang, X. Yin, and X. Zhang, Nat. Commun. **5**, 4316 (2014).
[8] S. Fu, Y. Tsur, J. Zhou, L. Shemer, and A. Arie, Phys. Rev. Lett. **115**, 034501 (2015).
[9] U. Bar-Ziv, A. Postan, and M. Segev, Phys. Rev. B **92**, 100301 (2015).
[10] B. A Malomed, D. Mihalache, F. Wise, and L. Torner, J. Opt. B **7**, R53 (2005).
[11] V. I. Kruglov, A. C. Peacock, J. M. Dudley, and J. D. Harvey, Opt. Lett. **25**, 1753 (2000).
[12] M. E. Fermann, V. I. Kruglov, B. C. Thomsen, J. M. Dudley, and J. D. Harvey, Phys. Rev. Lett. **84**, 6010 (2000).
[13] D. Anderson, M. Desaix, M. Karlsson, M. Lisak, and M. L. Quiroga-Teixeiro, J. Opt. Soc. Am. B **10**, 1185 (1993).
[14] S. Saghafi and C. J. R Sheppard, Opt. Commun. **153**, 207 (1998).
[15] S. Saghafi, C. J. R Sheppard, and J. A. Piper, Opt. Commun. **191**, 173 (2001).
[16] V. V. Kotlyar, A. A. Kovalev, and A. P. Porfirev, Opt. Lett. **40**, 701 (2015).
[17] T. Ellenbogen, I. Dolev, and A. Arie, Opt. Lett. **33**, 1207 (2008).
[18] A. Shapira, R. Shiloh, I. Juwiler, and A. Arie, Opt. Lett. **37**, 2136 (2012).
[19] K. Kalinowski, A. Shapira, A. Libster-Hershko, and A. Arie, Opt. Lett. **40**, 13 (2015).
[20] N. Olivier and E. Beaurepaire, Opt. Express **16**, 14703 (2008).
[21] K. B. Dysthe, Proc. R. Soc. A **369**, 105 (1979).
[22] L. G. Gouy, Ann. Chim. Phys. Ser. 6 **24**, 145 (1891).
[23] A. B. Ruffin, J. V. Rudd, J. F. Whitaker, S. Feng, and H. G. Winful, Phys. Rev. Lett. **83**, 3410 (1999).
[24] N. C. R. Holme, B. C. Daly, M. T. Myaing, and T. B. Norris, Appl. Phys. Lett. **83**, 392 (2003).
[25] G. Guzzinati, P. Schattschneider, K. Y. Bliokh, F. Nori, and J. Verbeeck, Phys. Rev. Lett. **110**, 093601 (2013).
[26] T. C. Petersen, D. M. Paganin, M. Weyland, T. P. Simula, S. A. Eastwood, and M. J. Morgan, Phys. Rev. A **88**, 043803 (2013).
[27] E. Lo and C. C. Mei, J. Fluid Mech. **150**, 395 (1985).
[28] L. Shemer and B. Dorfman, Nonlin. Processes Geophys. **15**, 931 (2008).
[29] E. Kit and L. Shemer, J. Fluid Mech. **450**, 201 (2002).
[30] E. R. Andresen, C. Finot, D. Oron, and H. Rigneault, Phys. Rev. Lett. **110**, 143902 (2013).
[31] S. Fu, Y. Tsur, J. Zhou, L. Shemer, and A. Arie, Phys. Rev. Lett. **115**, 254501 (2015).

[32] L. Shemer, K. Goulitski, and E. Kit, Eur. J. Mech. B, Fluids **26**, 193 (2007).
[33] L. Shemer, H. Jiao, E. Kit, and Y. Agnon, J. Fluid Mech. **427**, 107 (2001).
[34] A. E. Siegman, *Lasers* (University Science Books, Mill Valley, CA, 1986).
[35] L. Allen, M. W. Beijersbergen, R. J. C. Spreeuw, and J. P. Woerdman, Phys. Rev. A **45**, 8185 (1992).
[36] A. Chabchoub, N. Hoffmann, M. Onorato, G. Genty, J. M. Dudley, and N. Akhmediev, Phys. Rev. Lett. **111**, 054104 (2013).
[37] A. Chabchoub, B. Kibler, C. Finot, G. Millot, M. Onorato, J. M. Dudley, and A. V. Babanin, Ann. Phys. **361**, 490 (2015).